Spin and lattice dynamics in the van der Waals antiferromagnet MnPSe₃

Junbo Liao [ID],[1] Zhentao Huang [ID],[1] Yanyan Shangguan [ID],[1] Bo Zhang,[1] Shufan Cheng,[1] Hao Xu,[1] Ryoichi Kajimoto [ID],[2]
Kazuya Kamazawa,[3] Song Bao [ID],[1,*] and Jinsheng Wen [ID][1,4,†]

[1]*National Laboratory of Solid State Microstructures and Department of Physics, Nanjing University, Nanjing 210093, China*
[2]*J-PARC Center, Japan Atomic Energy Agency (JAEA), Tokai, Ibaraki 319-1195, Japan*
[3]*Neutron Science and Technology Center, Comprehensive Research Organization for Science and Society (CROSS),
Tokai 319-1106, Ibaraki, Japan*
[4]*Collaborative Innovation Center of Advanced Microstructures, Nanjing University, Nanjing 210093, China*

Antiferromagnetic van der Waals family MPX_3 ($M =$ Fe, Mn, Co, and Ni; $X =$ S and Se) have attracted significant research attention due to the possibility of realizing long-range magnetic order down to the monolayer limit. Here, we perform inelastic neutron scattering measurements on single-crystal samples of MnPSe₃, a member of the MPX_3 family, to study the spin dynamics and determine the effective spin model. The excited magnon bands are well characterized by a spin model, which includes a Heisenberg term with three intraplane exchange parameters ($J_1 = -0.73$ meV, $J_2 = -0.014$ meV, $J_3 = -0.43$ meV) and one interplane parameter ($J_c = -0.054$ meV), and an easy-plane single-ion anisotropy term ($D = -0.035$ meV). Additionally, we observe the intersection of the magnon and phonon bands but no anomalous spectral features induced by the formation of magnon-phonon hybrid excitations at the intersecting region. We discuss possible reasons for the absence of such hybrid excitations in MnPSe₃.

I. INTRODUCTION

The successful exfoliation of monolayer graphene has ushered in a new era of research in van der Waals (vdW) materials [1]. Over the past two decades, extensive research on atomic-thin vdW materials has led to the discovery of a wealth of fascinating physical phenomena, as well as tuning and controlling methods [2–5]. In recent years, the realization of intrinsic two-dimensional (2D) magnetism has established magnetic vdW materials as a promising platform for both application and fundamental research [6–8]. According to the Mermin-Wagner theorem, enhanced fluctuations will prevent the formation of long-range magnetic order in an isotropic low-dimensional magnetic system ($d < 3$) [9]. Therefore, the key to achieving intrinsic 2D magnetism lies in the exfoliation of bulk magnetic vdW materials with magnetic anisotropy down to the monolayer limit [6–8]. Presently, several classes of magnetic vdW materials have demonstrated intrinsic 2D magnetism, including vdW ferromagnets such as Cr₂Ge₂Te₆ [7], Fe₃GeTe₂ [10,11], and CrX_3 ($X =$ Cl, Br, I) [6,8], and vdW antiferromagnets like MPX_3 ($M =$ Fe, Mn, Co, Ni; $X =$ S, Se) [12,13].

As an early-discovered antiferromagnetic vdW family [14–17], MPX_3 ($M =$ Fe, Mn, Co, Ni; $X =$ S Se) have been extensively studied. Compounds in this family share the same hexagonal monolayer structure [Fig. 1(a)]. Each [P₂X_6]⁴⁻ unit is located in the center of nearby six M^{2+} ions. These M^{2+} ions connected to X atoms form a honeycomb structure, and the atomic layers are weakly coupled through the vdW force. Although these compounds all exhibit an antiferromagnetic order, the magnetic ground state and effective spin model vary significantly when varying the transition-metal ions M^{2+}. For example, MnPS₃ exhibits a Néel-type spin order and fits well a Heisenberg model [16–22]. On the other hand, FePS₃ and FePSe₃ exhibit a zigzag order and fit an Ising model [12,16,17,23–26]. CoPS₃ and NiPS₃ also display a zigzag order but are better described by an XY-like model [19,27–30]. This antiferromagnetic vdW class also provides a platform for tuning the 2D magnetism through doping [31,32], pressure [33,34], and strain [13], rendering these materials promising application potentials. Moreover, research on the atomic-thin sample reveals exotic physics, such as novel exciton behaviors in NiPS₃ [35,36] and magnon-phonon hybrid excitations, also known as magnon polarons in FePS₃ [37,38] and FePSe₃ [39].

MnPSe₃ is a member of the MPX_3 class. It exhibits a Néel-type antiferromagnetic order with a transition temperature $T_N \simeq 74 \pm 2$ K [16]. Neutron diffraction studies have confirmed a $k = (0, 0, 0)$ propagation vector, with the spin moments lying within the a-b plane when the compound is in its antiferromagnetic phase [31,40]. Although the spin ground state of MnPSe₃ has been determined, its effective spin model remains unclear. While some studies suggest an XY model [13,41], an inelastic neutron scattering (INS) investigation on powder samples leans towards a Heisenberg model [42]. Due to the lack of quantitative and detailed information on the momentum dependence of the spin dynamics, it is challenging to determine the effective spin model based on the results from powder samples. Therefore, detailed INS

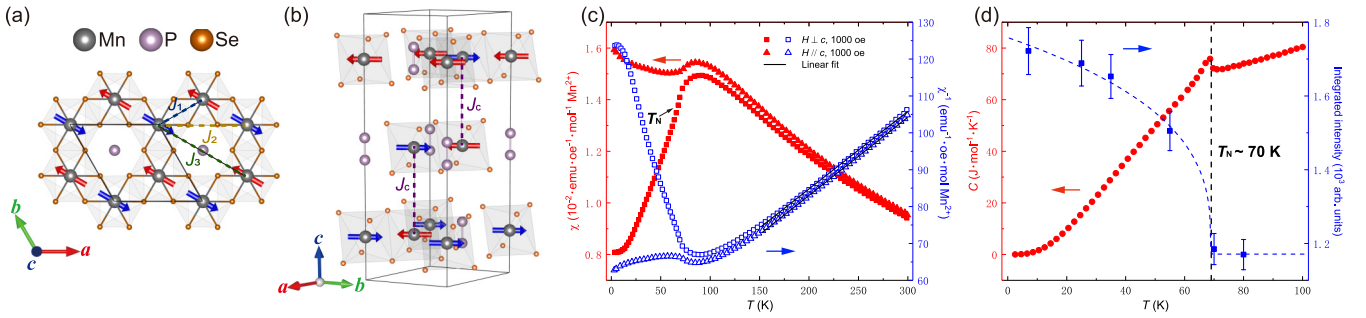*Contact author: songbao@nju.edu.cn
†Contact author: jwen@nju.edu.cn

FIG. 1. (a) Top view of the hexagonal structure of MnPSe$_3$ in the *a-b* plane. Arrows indicate the magnetic moments on Mn atoms. Dashed lines indicate the paths for the magnetic exchange interactions. (b) Schematic structures of the primitive cell of MnPSe$_3$. (c) Temperature dependence of the magnetic susceptibility χ (filled symbols, left axis) and the inverse magnetic susceptibility χ^{-1} (open symbols, right axis) with field applied parallel and perpendicular to the *c*-axis. Solid lines and the arrow denote the Curie-Weiss fit of χ^{-1} and the Néel transition temperature, respectively. (d) Temperature dependence of the specific heat C (circles, left axis) and the integrated intensity of $(-1, 0, 1)$ Bragg peak (squares, right axis). Error bars represent one standard deviation. The vertical dashed line indicates the Néel transition temperature. The dashed curve through the integrated intensities is a guide to the eyes.

research on the single-crystal samples is desired to determine the accurate effective spin model of MnPSe$_3$. In addition, a Raman spectroscopy study reported the observation of coupling between magnons and the optical phonons in MnPSe$_3$, indicating the presence of magnon polarons [43]. Since neutron spectroscopy can probe both magnons and phonons in the momentum-energy space [44,45], it is an ideal method to detect the possible magnon polarons.

In this work, we carry out INS experiment on single-crystal samples of MnPSe$_3$. We obtain clear magnon bands that exhibit a quasi-2D nature. We find that an effective spin model with three intraplane exchange parameters ($J_1 = -0.73$ meV, $J_2 = 0.014$ meV, $J_3 = -0.43$ meV), one interplane parameter ($J_c = -0.054$ meV), and one easy-plane single-ion anisotropy term ($D = -0.035$ meV) describes well the spin dynamics. Additionally, we find that the quasi-2D magnon bands intersect with a phonon band in the vicinity of (0, 0, 6), but no evidence of magnon-phonon coupling and the subsequent formation of magnon polarons has been detected. We discuss possible reasons for why these are absent in MnPSe$_3$.

II. EXPERIMENTAL DETAILS

The crystal structure of MnPSe$_3$ belongs to the space group $R\bar{3}$ (No. 148), which consisted of three hexagonal atomic layers arranged in an ABC-type stacking within a unit cell, as shown in Figs. 1(a) and 1(b). The lattice parameters are $a = b = 6.387$ Å and $c = 19.996$ Å [16]. Single crystals of MnPSe$_3$ were grown by the chemical vapor transport method [41,46]. As-grown MnPSe$_3$ crystals appeared as thin wine-red flakes and were easy to bend and cut. The typical size of the single crystals was about $5 \times 5 \times 0.1$ mm^3. Magnetization and specific-heat measurements were conducted in a physical property measurement system (PPMS-9T) from Quantum Design.

For the INS experiments, we glued 140 pieces of single crystals onto aluminum plates using a trademarked fluoropolymer CYTOP-M, with a total weight of 1.86 g. The orientations of the crystals were determined using a backscattering Laue x-ray diffractometer. The single crystals were mounted on the rectangular aluminum plates, with the

[100] and [−120] axes aligned along the edge directions of the aluminum plate. The coaligned sample had a mosaic spread of $2°$.

The INS experiment was conducted on a time-of-flight spectrometer 4SEASONS at the Materials and Life Science Experimental Facility of the J-PARC Center in Japan [47]. We used a primary energy of $E_i = 14.00$ meV and a chopper frequency of 300 Hz to conduct the measurements, resulting in an energy resolution of 0.6 meV at the elastic line. Thanks to the multiple-E_i mode equipped on 4SEASONS, we also obtained data with other E_i's of 7.87, 10.29, and 20.19 meV, with the respective energy resolution of 0.3, 0.4, and 0.9 meV at the elastic positions [48]. We set the angle of the incident neutron beam direction parallel to the *c*-axis to be zero. Scattering data were collected by rotating the sample about the [−120] direction in a step of $1°$ from $-50°$ to $180°$ at 6 K, and from $0°$ to $105°$ at 150 K. At both temperatures, we counted 15 min for each step. In addition, measurements were also performed at seven other temperatures of 25, 35, 55, 70, 80, and 120 K. At these temperatures, we fixed the angle to be $0°$ and counted 1 h for this angle. Raw data were reduced and analyzed using Utsusemi and Horace software [49,50]. The wave vector $\mathbf{Q}$ was expressed as (H, K, L) reciprocal-lattice unit (rlu) of $(a^*, b^*, c^*) = (4\pi/\sqrt{3}a, 4\pi/\sqrt{3}b, 2\pi/c)$. We corrected the measured neutron scattering intensity by dividing the square of the magnetic form factor $|F(\mathbf{Q})|^2$ of Mn^{2+} ions. The corrected data were further divided by the Bose factor via $\chi''(\mathbf{Q}, \omega) = (1 - e^{-\hbar\omega/k_B T})S(\mathbf{Q}, \omega)$ to eliminate the influence of the Bose statistics, where k_B is the Boltzmann factor. Theoretical simulations of the excitation spectra were performed using the SPINW program [51].

III. RESULTS

A. Sample characterizations

We have conducted the magnetic susceptibility measurements on a single crystal of MnPSe$_3$ with a 0.1-T field applied for both in-plane and out-of-plane directions, and the results are shown in Fig. 1(c). Upon cooling, we observe little difference in the magnetic susceptibility between the two directions in the paramagnetic phase

$(T > 120$ K$)$, similar to that in MnPS$_3$ as reported in Refs. [19] and [41], indicating a weak magnetocrystalline anisotropy in MnPSe$_3$. We have also noted that in Ref. [41], a large anisotropy over the entire temperature range was reported for MnPSe$_3$. We have measured several single crystals that we grew, and all of them show similar results to those in Fig. 1(c). As we will discuss in detail below, this weak anisotropy is consistent with our neutron scattering results. In the vicinity of 100 K, the susceptibility displays a broad peak, which is a typical feature of low-dimensional magnetic systems [19]. This peak is ascribed to the establishment of short-range spin-spin correlations among the magnetic moments in the materials [19]. At lower temperatures, long-range magnetic order occurs, as evidenced by the kink point around 70 K in the magnetic susceptibility curves [Fig. 1(c)]. This magnetic phase transition at $T_N \simeq 70$ K is further supported by the λ-type anomaly observed in the specific-heat measurements and the onset of magnetic scattering intensities at the magnetic Bragg peak $(-1, 0, 1)$ as observed in the neutron scattering measurements [Fig. 1(d)]. Upon further cooling, the in-plane susceptibility dramatically decreases, while the out-of-plane susceptibility slightly increases [Fig. 1(c)]. Such behaviors indicate that MnPSe$_3$ establishes a collinear antiferromagnetic order with the magnetic moments lying in the a-b plane, which is consistent with previous neutron diffraction results [16,42].

To quantitatively understand the magnetic susceptibility results, we fit the data above 150 K using the Curie-Weiss law, $1/\chi = (T + \Theta)/C$, where C and Θ are the Curie constant and Curie-Weiss temperature, respectively [Fig. 1(c)]. The extracted Curie constants are 4.72 and 4.75 emu K/mol Mn^{2+}, and the resulting effective magnetic moments of $6.14\mu_B$ and $6.16\mu_B$ for $H||c$ and $H \perp c$, respectively. These results indicate a high spin state of $S = 5/2$ for Mn^{2+} ions and a Landé g factor of 2.08 with a negligible spin-orbit coupling in this material. The fitted Curie-Weiss temperatures are $\Theta_\parallel = -192.06$ K and $\Theta_\perp = -203.10$ K, respectively, demonstrating strong antiferromagnetic correlations in MnPSe$_3$.

B. Magnon spectra

Although the crystal structure of MnPSe$_3$ possesses a $\bar{C}_3$ axis, the Laue pattern shows a nearly C_6 symmetry, which makes it difficult to distinguish two kinds of sample alignments rotated by $60°$. Due to the $\bar{C}_3$ axis, these two alignments are equivalently connected by the mirror operation about the a-b plane. Therefore, the data we have collected with a nominal $\mathbf{Q} = (H, K, L)$ correspond to a superposition of the actual signals at (H, K, L) and $(H, K, -L)$, which we call the "twinned" effect. This can be confirmed by comparing the distribution of experimentally measured and theoretically predicted magnetic Bragg peaks in the $(H, 0, L)$ plane. Figure 2(a) shows the measured magnetic Bragg peaks in the $(H, 0, L)$ plane. Given that the spin moments in the sublattice of each layer align parallel to those in the adjacent layers, and the number of layers per unit cell being three, the magnetic Bragg peaks are expected to be located at integer positions of L with a periodicity of 3 rlu along the [001] direction, which is indeed observed in Fig. 2(a). These peaks are symmetrically distributed about the $L = 0$ line. Figure 2(b) shows the
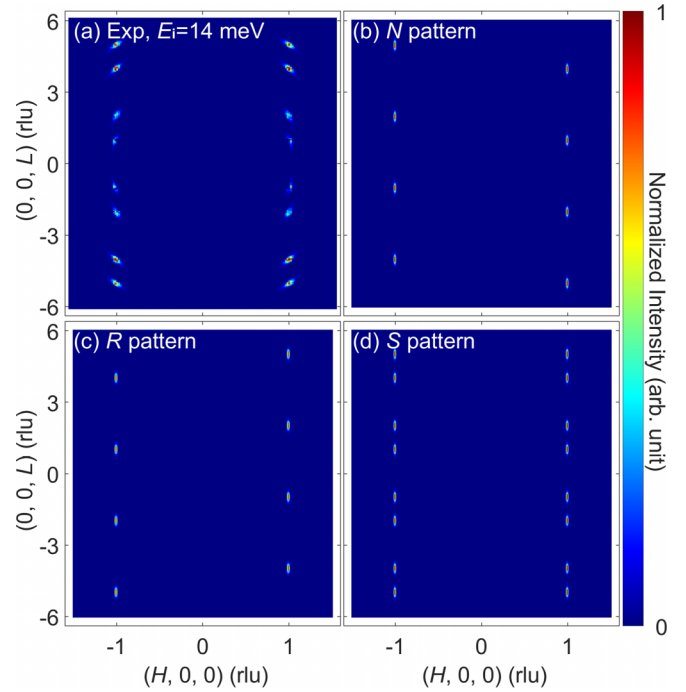

FIG. 2. (a) Measured magnetic Bragg peaks in the $(H, 0, L)$ plane with the incident energy of $E_i = 14$ meV for MnPSe$_3$. The energy is integrated over $[-0.1, 0.1]$ meV. The lattice contributions are eliminated by subtracting the data of 150 K. (b) Theoretically calculated magnetic Bragg peaks in the $(H, 0, L)$ plane according to the untwinned case, termed the N pattern. (c) Reflection of the N pattern about the $L = 0$ line, termed the R pattern. (d) Superposition of the patterns in (b) and (c), termed the S pattern, representing the magnetic Bragg scatterings from the twinned sample.

theoretically calculated distribution of the magnetic Bragg peaks without taking into account the twinned effect. Different from the experimental results, the calculated pattern does not show reflection symmetry about the $L = 0$ line but instead exhibits centrosymmetry about the origin $(0, 0, 0)$. For clarity, we refer to this pattern as the N pattern, where N stands for "normal." In Fig. 2(c), we present the reflected results of the N pattern about the $L = 0$ line, and we refer to it as the R pattern. The comparable intensities observed in the two sets of magnetic Bragg peaks in Fig. 2(a) suggest that the single crystals contributing to the N and R patterns are nearly equal. Therefore, we superpose these two patterns in a 1:1 ratio, and we call it an S pattern. The results are shown in Fig. 2(d). Obviously, the S pattern reproduces the experimental results well, supporting the conjecture regarding the sample twinning.

After clarifying the twinned issue of the sample alignment, we now present the spin excitation spectra of MnPSe$_3$. Figures 3(a) and 3(b) show the in-plane and out-of-plane spin excitation spectra, respectively. The paths for the in-plane spin excitation spectra are illustrated in the inset of Fig. 3(a). It is found that the well-defined magnon excitations disperse up from the zone center Γ point and propagate towards the zone boundary, with the maximum occurring around 8.5 meV, consistent with previous neutron scattering results from a powder sample [42]. This profile closely resembles that of its
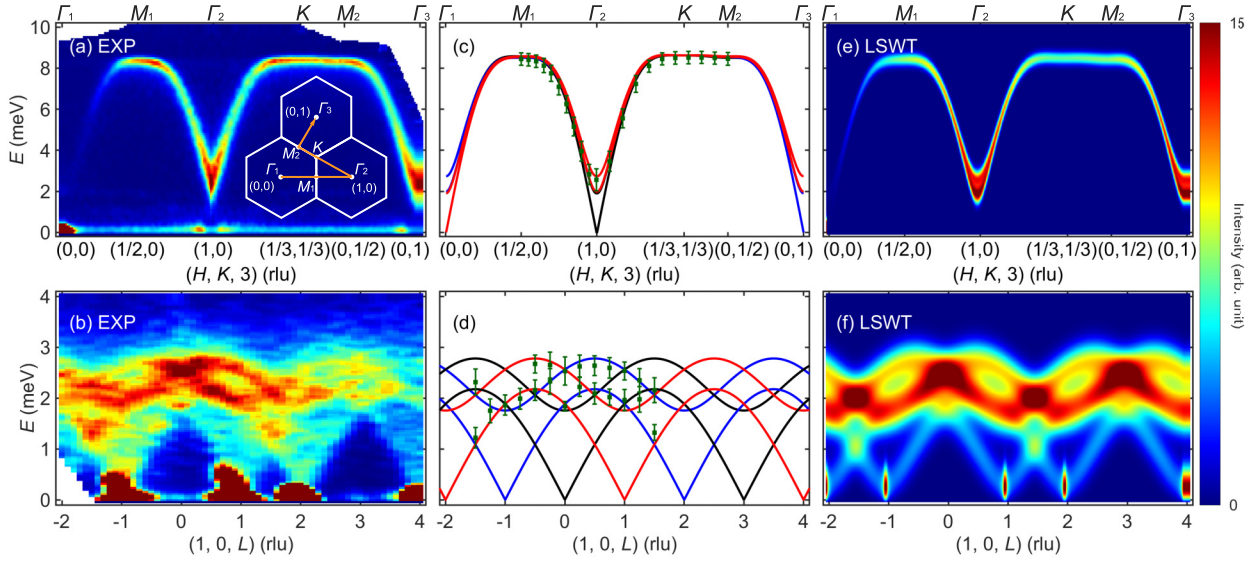
FIG. 3. INS results of the magnetic excitation spectra at 6 K along the in-plane (a) and out-of-plane (b) directions. The data were obtained with $E_i = 14$ meV for (a), and $E_i = 7.87$ meV for (b). In (a), the integration thickness of the other in-plane direction, orthogonal to the high-symmetry path, is chosen to be ± 0.05 rlu, and the wave vectors L are integrated over [2.5, 3.5] rlu. In (b), the integration range for the two orthogonal in-plane vectors is ± 0.05 rlu. (c),(d) Calculated in-plane and out-of-plane magnon dispersions using the linear spin-wave theory (LSWT), respectively. The data points are extracted from the experimental spectra presented in (a) and (b). (e),(f) Calculated magnetic excitation spectra, which are superposed with $\pm L$ cases taking into account the twinning effect and instrumental resolutions. The inset in (a) illustrates the high-symmetry paths of the in-plane excitation spectra.

sister compound MnPS$_3$, which has an 11.5-meV bandwidth, indicating remarkable intralayer exchange interactions [21]. It is noteworthy that the magnons exhibit an onset of excitations around 1.8 meV for $L = 3$ rlu [Fig. 3(a)]. However, this does not indicate an excitation gap but is attributed to the out-of-plane variations of the magnetic excitations, which mainly modify the bottom of the magnon dispersions. This can be visualized from the excitations along the $[1, 0, L]$ direction as plotted in Fig. 3(b). Note that the out-of-plane spectra show remarkable broadening in momentum, which indicates the weak correlations along L due to the two-dimensionality. Similar to the elastic patterns shown in Fig. 2(a), these excitations show an $L = 3$ rlu period. In the range of $L = [-1, 1]$ rlu, two winding bands can be recognized in the energy range of [1.9, 2.8] meV. As will be confirmed in the next section, these two bands actually correspond to N and R bands due to the sample twinning along the L direction. In addition, the spectral weight is continuously distributed towards the magnetic Bragg peaks at $(1, 0, \pm 1 + 3n)$ rlu. Although the detailed spectra below 0.3 meV are obscured by the strong and elongated signal of the magnetic Bragg peaks, making it difficult to determine whether there is an excitation gap, our data sets an upper bound of the excitation gap of 0.3 meV. Moreover, a recent study employing magnetospectroscopy reported the gap will be less than 0.1 meV, if it does exist [52].

C. Effective spin model

To capture the observed features of the well-defined magnons and determine the effective spin model, we employ the following spin Hamiltonian to model our data, considering

the easy-plane magnetic order:

$$H = -\sum_{\langle i,j \rangle} J_{i,j} \boldsymbol{S}_i \cdot \boldsymbol{S}_j - \sum_{\langle i \rangle} D_i \big(S_i^z \big)^2. \qquad (1)$$

Here, S_i is the spin operator of a Mn^{2+} ion at the site $\boldsymbol{r}_i$ with a magnitude of 5/2, $J_{i,j}$ is the exchange interaction connecting two Mn^{2+} ions at sites $\boldsymbol{r}_i$ and $\boldsymbol{r}_j$, and D_i is the single-ion anisotropy of Mn^{2+} ions. We take three intralayer exchange interactions (nearest-neighbor interaction J_1, next-nearest-neighbor interaction J_2, and third-nearest-neighbor interaction J_3) and one interlayer exchange interaction (J_c) into consideration in the parametrization. A detailed configuration of these interactions is given in Figs. 1(a) and 1(b). We use the SPINW package to model our data with the linear spin-wave theory (LSWT) [51,53]. In this approach, a standard Holstein-Primakoff transformation is applied to Eq. (5) to get a 12×12 matrix that characterizes the spin dynamics of MnPSe$_3$. The dispersion relation $\hbar\omega(\boldsymbol{Q})$ is obtained by a Bogoliubov transformation on the 12×12 matrix.

To determine the specific exchange parameters $J_{i,j}$ and single-ion anisotropy D_i, we first make constant-$\boldsymbol{Q}$ cuts through the excitation spectra in Figs. 3(a) and 3(b) at various momenta and fit these cuts with Gaussian line shapes to extract the magnon energies. By doing so, we can obtain the magnon dispersion. Subsequently, we fit the extracted dispersion relation with a theoretical $\hbar\omega(\boldsymbol{Q})$ function. In this procedure, we restrict D_i to be negative to remain consistent with the easy-plane anisotropy, revealed by the easy-plane magnetic order and negligible excitation gap [52]. The refined exchange parameters are presented in the first row of Table I, where the additional parameter χ^2 evaluates the goodness of

TABLE I. The fitting exchange parameters obtained from the current work on single-crystal samples and reported results from powder samples in Ref. [42]. Errors represent one standard deviation. The goodness of fit is represented by the value of χ^2, where a value closer to 1 indicates a better fit.

Paper	Model	J_1 (meV)	J_2 (meV)	J_3 (meV)	J_c (meV)	D (meV)	δ	χ^2
Current work	Heisenberg + D	-0.73 ± 0.03	-0.014 ± 0.005	-0.43 ± 0.04	-0.054 ± 0.005	-0.035 ± 0.004		1.5
Current work	Heisenberg	-0.74 ± 0.03	-0.017 ± 0.005	-0.41 ± 0.05	-0.075 ± 0.004			2.4
Ref. [42]	Heisenberg	-0.9	-0.06	-0.38	-0.062			3.8
Current work	XXZ	-0.73	-0.014	-0.43	-0.054		0.981	

fit in the SPINW program. Some extracted experimental points and the calculated dispersions with the refined parameters are plotted in Figs. 3(c) and 3(d). The calculated dispersions fit the extracted experimental points quite well. With the involved magnetic parameters, the calculations give six magnon bands, consistent with the six magnetic ions in a unit cell. These six bands can be divided into three groups, denoted by red, blue, and black in Figs. 3(c) and 3(d). Each group consists of one acoustic and one optical branch. These three dispersion groups have the same shape, but are shifted by $\Delta L = 1$ rlu from each other along the [001] direction, which can be visualized from Fig. 3(d).

To directly compare the intensities with the experimental results, we calculate the dynamical spin-spin correlation function [44,45],

$$S^{\alpha\beta}(\boldsymbol{Q}, \omega) = \frac{1}{2\pi} \sum_l e^{i\boldsymbol{Q}\cdot\boldsymbol{r}_l} \int_{-\infty}^{\infty} \langle S_0^\alpha(0) S_l^\beta(t) \rangle e^{-i\omega t} dt. \quad (2)$$

$S^{\alpha\beta}(\boldsymbol{Q}, \omega)$ is related to the scattering cross section as

$$\frac{d^2\sigma}{d\Omega d\omega} \propto |\boldsymbol{F}(\boldsymbol{Q})|^2 \sum_{\alpha\beta} \left(\delta_{\alpha\beta} - \frac{Q_\alpha Q_\beta}{Q^2} \right) S^{\alpha\beta}(\boldsymbol{Q}, \omega), \quad (3)$$

which is directly measured in INS experiments. The calculated results of $S^{\alpha\beta}(\boldsymbol{Q}, \omega)$ show that only the two bands in the red group possess significant spectral weight, while the remaining two groups are invisible in principle. However, due to the twinning effect as discussed above, there actually exist two groups of excitation spectra symmetrized about $L = 0$ that possess scattering intensities, as shown in Fig. 3(b). To reproduce the magnetic excitation spectra observed in the twinned sample, we convolute the instrumental resolution with the calculated $S^{\alpha\beta}(\boldsymbol{Q}, \omega)$ and superpose the N and R patterns of the excitations, which mainly affect the out-of-plane excitations. The final calculated magnon spectra of MnPSe$_3$ are presented in Figs. 3(e) and 3(f). For the in-plane direction, the calculated excitation spectra successfully capture the shape of the measured spectra. In addition, the dynamical spin structure factor along Γ_1 to M_1 is significantly smaller than that along Γ_3 to M_2 in the calculated spectra, which is in excellent agreement with the experimental observations shown in Fig. 3(a). Note that the calculated spectra exhibit weaker intensity at the top of the magnon band compared to the measured one. This discrepancy should stem from the mismatch between the resolution function and magnon dispersion in the INS experiment, which is not considered in the calculations. In terms of the out-of-plane spectra, our calculations successfully capture the major features of the experimental spectra, especially the two winding bands around

the band top. On the other hand, to reproduce the broadening of the measured spectra along the L direction, one may need to take into account the two-dimensionality. These successful reproductions of the experimental data further validate the accuracy and reliability of our approach in characterizing the spin dynamics of MnPSe$_3$.

D. Magnon-phonon intersection

In addition to magnons, our INS experiment also allows us to probe phonons. This capability enables us to examine whether there exist magnon polarons induced by the coupling between magnons and phonons in MnPSe$_3$, as proposed in its sister compounds FePS$_3$ and FePSe$_3$ [37–39]. Direct spectroscopic evidence of magnon polarons is the gap opening at the nominal intersection of the original magnon and phonon bands, accompanied by the mixing and interconversion of magnonic and phononic characters [37–39,54–60]. Therefore, the key to addressing this issue lies in identifying the region where magnons and phonons intersect with each other. Figure 4(a) shows the constant-energy (E) contour around 5 meV in the $(H, 0, L)$ plane. Two rodlike excitations of magnons are clearly observed with negligible L dependence, which reflects the quasi-2D nature of magnetic excitations due to the weak interlayer exchange interaction. Additionally, the oval-like excitations centered at $(0, 0, 6)$ are also visible, intersecting with the rodlike excitations in regions with L around 4.7 and 7.3 rlu, as marked by the dashed lines in Fig. 4(a). These two L's are symmetric about $L = 6.0$ rlu. We attribute these distinct excitations with a 3D nature to a phonon mode. Notably, the intensities of the rodlike excitations remain constant with increasing L, while those of the oval-like excitations increase [Fig. 4(a)]. Such behaviors are consistent with the characteristics of the magnetic form-factor-corrected magnons and phonons, respectively.

To examine the intersection of the magnon and phonon dispersions, we select the region with $L = 4.7$ rlu, where the scattering intensities of magnons and phonons are comparable [Fig. 4(a)], and we plot the excitation spectra along the [100] direction in Fig. 4(b). In this plot, two distinct dispersions can be clearly identified within the same momentum-energy window: a V-shaped magnon dispersion starting from 3 meV, and a W-shaped phonon dispersion distributed above 4.3 meV. The magnon and phonon dispersions appear to intersect at about $H = \pm 0.15$ rlu. However, within the instrumental resolution, there are no apparent gap openings at these intersections. To verify whether the magnon and phonon dispersions are distorted or renormalized due to the possible magnon-phonon coupling [37–39,54–60], we investigate the
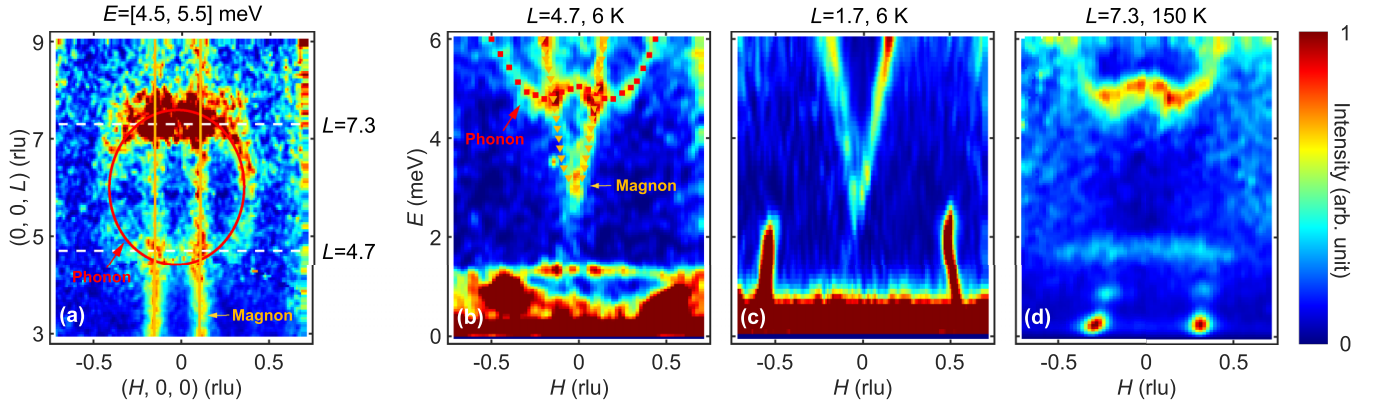
FIG. 4. (a) Constant-E contour at 5 meV in the $(H, 0, L)$ plane, obtained with $E_i = 10.29$ meV. The integration thickness of the energy is ± 0.5 meV. Lines and the oval denote magnon excitations and phonon excitations, respectively. The dashed lines indicate the L positions where the magnon and phonon dispersions intersect with each other. (b) The overlapped magnon and phonon excitations at 6 K presented in the same momentum-energy window with $L = 4.7$ meV. Triangles and squares denote magnon and phonon dispersions extracted from (c) and (d), respectively. (c),(d) The individual magnon and phonon spectra, obtained with $L = 1.7$ rlu at 6 K and $L = 7.3$ rlu at 150 K, respectively. The integration thicknesses of the [−120] and [001] directions are ± 0.1 and ± 0.15 rlu, respectively.

individual magnon and phonon dispersions in Figs. 4(c) and 4(d), respectively. By deceasing L, we effectively suppress the scattering intensities of phonons, and we plot the pure magnons at a symmetrically equivalent position of $L = 1.7 = 4.7 − 3.0$ rlu at 6 K in Fig. 4(c). On the other hand, by increasing the temperature to 150 K, well above the T_N, we obtain pure phonons at a higher intersection position with $L = 7.3$ rlu in Fig. 4(d). The momentum-energy relationships of the individual magnons [Fig. 4(c)] and phonons [Fig. 4(d)] are extracted by doing either constant-$\boldsymbol{Q}$ or constant-E cuts through the excitation spectra. These extracted points are plotted over the spectra, with triangles and squares representing pure magnons and phonons, respectively, as shown in Fig. 4(b). It is found that the extracted magnon and phonon bands match the overlapped magnon and phonon dispersions well, suggesting that there is no normalization between magnons and phonons. In other words, we find no obvious evidence of magnon polarons in MnPSe$_3$.

IV. DISCUSSIONS

A. Easy-plane anisotropy

We observe clear magnon dispersions in MnPSe$_3$ through INS experiments. To determine the effective spin model, we employ a Hamiltonian including a Heisenberg term and an easy-plane single-ion anisotropy (D) term to fit our INS data. Our theoretical fit gives a weak easy-plane anisotropy with a value of $−0.035$ meV. To estimate the significance of the easy-plane anisotropy and address the controversy regarding the effective spin model of MnPSe$_3$ [13,41,42], we fit the experimental data with the Heisenberg term only. The exchange parameters given by the optimal fitting are presented in the second row of Table I. The goodness of fit χ^2 is 2.4, which is larger than that with the D term. Table I also lists the exchange parameters in a Heisenberg model from a previous INS measurement on powder samples [42]. It should be noted that since the definition of the spin Hamiltonian differs by a factor of 2, the parameters obtained from Ref. [42] are multiplied by 2 to maintain consistency with our definition. We

attempt to fit our data with their parameters, and the resulting value of χ^2 is 3.8, also larger than the value with a D term. Obviously, including the D term yields a better fitting. More importantly, the presence or absence of the D term results in qualitatively different magnon spectra. Figures 5(a) and 5(b) show the calculated magnon spectra with and without the D term, respectively. The twinning effect is not taken into consideration for brevity. The calculated spectra with the D term exhibit two magnon bands, including one acoustic and one optical branch as described previously, while the spectra without the D term only exhibit one magnon band dispersing from 0 to 3 meV, which makes it deviate from the measured spectra shown in Fig. 3(b). To further illustrate this, we extract the measured energy distribution of the intensity at $\boldsymbol{Q} = (1, 0, −3/2)$ and plot it in Fig. 5(c), which clearly shows two peaks at about 1.1 and 2.3 meV. Then, we fit the measured distribution with the Heisenberg + D model and the Heisenberg model, respectively. It is apparent that the Heisenberg + D model successfully captures the two-peak feature, while the Heisenberg model fails to characterize the peak at 2.3 meV. Therefore, we believe that the easy-plane anisotropy, though weak, must be included to properly describe the spin dynamics of MnPSe$_3$. The inclusion of this term is also consistent with the easy-plane magnetic order [13,40,41].

B. Connection with the XXZ model

To take the easy-plane anisotropy into consideration, we can also adopt the following XXZ model:

$$H = -\sum_{\langle i,j \rangle} J_{i,j}\left(S_i^x S_j^x + S_i^y S_j^y + \delta_{i,j} S_i^z S_j^z\right). \qquad (4)$$

Here, the easy-plane anisotropic nature can be guaranteed by restricting the anisotropy factor $\delta_{i,j}$ to be smaller than 1. Nevertheless, within the framework of LSWT, a Heisenberg + D model is equivalent to such an XXZ model in characterizing the spin dynamics [26,53]. The impact of all anisotropy factors $\delta_{i,j}$ in the XXZ model can be equivalently displayed by the D term in the Heisenberg + D model. In the case of
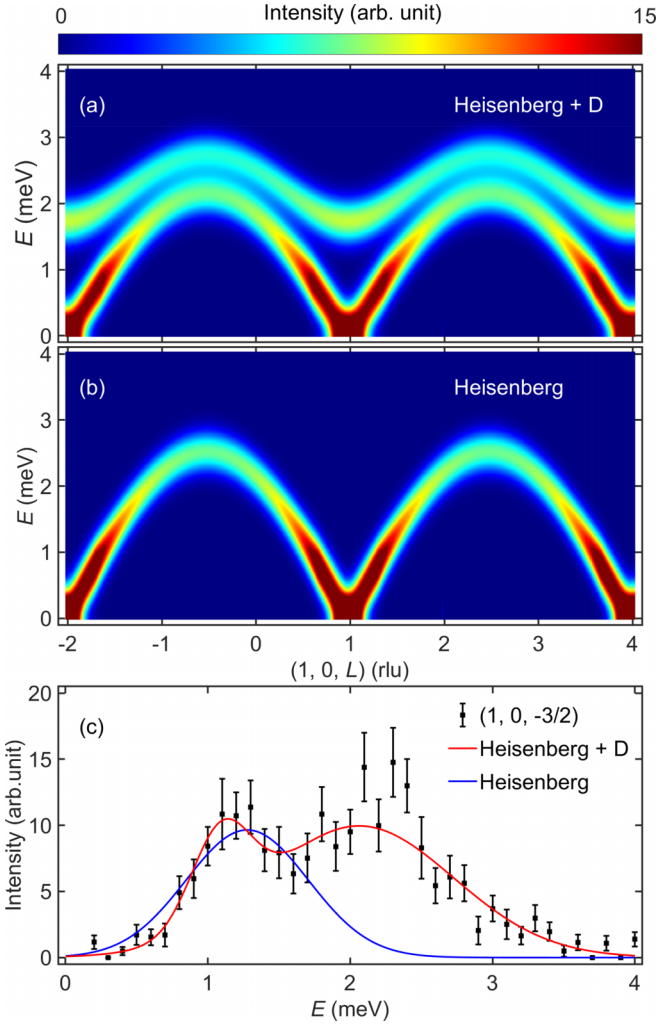
FIG. 5. (a),(b) Calculated magnon spectra with and without the D term, respectively. (c) Comparison between the measured energy distribution of the spectral weight with the calculations with and without the D term at $\boldsymbol{Q} = (1, 0, -3/2)$.

MnPSe$_3$, these two models can be linked by

$$D = \frac{3(1 - \delta_1)J_1 + 3(1 - \delta_2)J_2 + 3(1 - \delta_3)J_3 + (1 - \delta_c)J_c}{2}. \tag{5}$$

Here, δ_i with $\{i = 1, 2, 3, c\}$ corresponds to the anisotropy factor of the bond that we are concerned with in the Heisenberg + D model. If we only consider a global anisotropy factor δ, that is, $\delta_1 = \delta_2 = \delta_3 = \delta_c = \delta$, our refined D term with the value of -0.035 meV gives rise to an anisotropy factor $\delta = 0.981$ (Table I). The corresponding parameters of the XXZ model are listed in the fourth row of Table I. At present, we believe the Heisenberg + D or the equivalent XXZ model within the framework of LWST can already describe the magnetic excitation spectra well, but to further determine which one describes the spin dynamics of MnPSe$_3$ more precisely, one has to process the higher-order term beyond LSWT [53] or calculate the exchange parameters with first principles [29].

C. Magnetic excitations in MPX_3 compounds

Now, we would like to briefly review the magnetic excitations of the MPX_3 (M = Fe, Mn, Co, Ni; X = S, Se) compounds taking into account our results. The magnetic excitation spectra of FePS$_3$ and FePSe$_3$ exhibit similar magnon dispersions with large bandwidth ($\gtrsim$20 meV) and excitation gap ($\sim$15 meV) [25,26]. This gap demonstrates the presence of a large easy-axis anisotropy and Ising nature of the spin model [25,26]. INS experiments on CoPS$_3$ observed four clear spin-wave branches with a bandwidth of $\sim$18 meV and a large energy gap ($\gtrsim$14 meV), which can be well described by a model with a Heisenberg term and biaxial single-ion anisotropy [27,28]. Moreover, it is found that the dominating exchange interaction is the third-neighbor (3NN) antiferromagnetic interaction [27]. In the case of NiPS$_3$, INS experiments reported a wide magnetic excitation ($\gtrsim$45 meV) with a $\sim$1.3 meV excitation gap [29]. The LSWT fit also manifests a dominating 3NN exchange interaction, which stems from the large 3NN e_g-e_g hopping integrals confirmed by *ab initio* density functional theory calculations [29]. As we can see, MnPSe$_3$ and MnPS$_3$ are the two compounds that have the narrowest magnon bandwidth ($\sim$8.5 and $\sim$11.3 meV [21]) and the smallest excitation gap (less than $\sim$0.1 meV [52] and $\sim$0.5 meV [21]) in the MPX_3 material family. The weak spin-orbit coupling of Mn^{2+} ions is potentially responsible for the weak exchange interaction and magnetic anisotropy. Note that Mn^{2+} ions possess a half-filled $3d$ shell, resulting in a quenched $L = 0$ orbital moment.

D. Absence of magnon polarons

In addition to the clear magnon dispersions, we also observe the intersections between magnon and phonon dispersions. However, no obvious evidence of gap opening and hybridization between the two excitations has been identified in Fig. 4. This suggests that there is negligible magnon-phonon coupling in MnPSe$_3$, in contrast to the case in its sister compounds FePS$_3$ and FePSe$_3$ [37–39]. Since the magnetic interactions depend on the relative ion positions, magnon-phonon coupling can arise due to the lattice vibrations. There are various mechanisms with which magnon-phonon coupling can support magnon polarons, including magnetic dipolar interaction [54], magnetoelastic coupling [37,58–62], and Dzyaloshinskii-Moriya (DM) interactions [55,63,64]. While the strength of magnetic dipolar interaction is usually small compared to other interactions [65], its contribution is expected to be negligible in MnPSe$_3$. On the other hand, magnetic anisotropy plays a crucial role in magnetoelastic coupling [37,58–62]. However, in the case of MnPSe$_3$, the magnetic anisotropy appears to be very weak, as inferred from the results of magnetic susceptibility [Fig. 1(a)] and the excitation spectra [Fig. 3(b)]. Therefore, the mechanism of magnetoelastic coupling is not applicable in MnPSe$_3$. Additionally, the weak spin-orbit coupling results in the insignificance of the antisymmetric DM interaction in MnPSe$_3$, making the DM mechanism insufficient to open a gap between magnon and phonon dispersions and generate the magnon polarons.

While our INS measurements do not directly detect magnon-phonon coupling or magnon polarons between

one-magnon excitations and phonons, previous temperature-dependent magneto-Raman spectroscopy measurements have reported the presence of hybrid excitations involving two-magnon modes and optical phonon modes in MnPSe$_3$ [43]. This hybridization arises from the exchange striction effect, where the normal mode motion of the optical phonon mode modifies the distance between the nearest-neighbor and third-nearest-neighbor Mn^{2+} ions and affects the superexchange interactions J_1 and J_3 [43,66]. As the two-magnon modes and optical phonon modes overlap at the energy of about 16.2 meV, their coherent resonance induces the hybridization in MnPSe$_3$. However, due to the weak intensity of the two-magnon excitation for a spin-5/2 system [67], our INS measurements do not capture the two-magnon modes, which should appear as a weak continuum-like excitation above the one-magnon dispersion in the INS spectra [67–70]. Consequently, the hybrid excitations of the two-magnon and phonon modes are not observed.

V. CONCLUSIONS

We conduct comprehensive INS measurements on single-crystal samples of MnPSe$_3$ to study the spin dynamics and determine the effective spin model. Clear magnon bands are observed in our INS experiment. The excited magnon bands can be well described by an effective spin Hamiltonian with three intraplane exchange parameters ($J_1 = -0.73$ meV, $J_2 = -0.014$ meV, $J_3 = -0.43$ meV), one interplane parameter ($J_c = -0.054$ meV), and an easy-plane single-ion anisotropy ($D = -0.035$ meV). This model is equivalent to an *XXZ* model with a global anisotropy factor $\delta = 0.981$ in the framework of LSWT. Furthermore, we observe that a quasi-2D magnon mode intersects with a phonon mode which disperses from (0,0,6) rlu in the Brillouin zone. Nevertheless, none of the anomalous spectral features induced by magnon polarons have been identified in the intersection region, which we attribute to the weak spin-orbit coupling due to the quenched orbital momentum of Mn^{2+}.

[1] K. S. Novoselov, A. K. Geim, S. V. Morozov, D. Jiang, Y. Zhang, S. V. Dubonos, I. V. Grigorieva, and A. A. Firsov, Electric field effect in atomically thin carbon films, Science **306**, 666 (2004).

[2] S. Das Sarma, S. Adam, E. H. Hwang, and E. Rossi, Electronic transport in two-dimensional graphene, Rev. Mod. Phys. **83**, 407 (2011).

[3] Y. Liu, N. O. Weiss, X. Duan, H. Cheng, Y. Huang, and X. Duan, Van der Waals heterostructures and devices, Nat. Rev. Mater. **1**, 16042 (2016).

[4] X. Gu, Y. Wei, X. Yin, B. Li, and R. Yang, *Colloquium:* Phononic thermal properties of two-dimensional materials, Rev. Mod. Phys. **90**, 041002 (2018).

[5] A. Avsar, H. Ochoa, F. Guinea, B. Özyilmaz, B. J. van Wees, and I. J. Vera-Marun, *Colloquium:* Spintronics in graphene and other two-dimensional materials, Rev. Mod. Phys. **92**, 021003 (2020).

[6] B. Huang, G. Clark, E. Navarro-Moratalla, D. R. Klein, R. Cheng, K. L. Seyler, D. Zhong, E. Schmidgall, M. A. McGuire, D. H. Cobden *et al.*, Layer-dependent ferromagnetism in a van der Waals crystal down to the monolayer limit, Nature (London) **546**, 270 (2017).

[7] C. Gong, L. Li, Z. Li, H. Ji, A. Stern, Y. Xia, T. Cao, W. Bao, C. Wang, Y. Wang *et al.*, Discovery of intrinsic ferromagnetism in two-dimensional van der Waals crystals, Nature (London) **546**, 265 (2017).

[8] A. Bedoya-Pinto, J. Ji, A. K. Pandeya, P. Gargiani, M. Valvidares, P. Sessi, J. M. Taylor, F. Radu, K. Chang, and S. S. P. Parkin, Intrinsic 2D-XY ferromagnetism in a van der Waals monolayer, Science **374**, 616 (2021).

[9] N. D. Mermin and H. Wagner, Absence of ferromagnetism or antiferromagnetism in one- or two-dimensional isotropic heisenberg models, Phys. Rev. Lett. **17**, 1133 (1966).

[10] Y. Deng, Y. Yu, Y. Song, J. Zhang, N. Z. Wang, Z. Sun, Y. Yi, Y. Z. Wu, S. Wu, J. Zhu *et al.*, Gate-tunable room-temperature ferromagnetism in two-dimensional Fe$_3$GeTe$_2$, Nature (London) **563**, 94 (2018).

[11] S. Bao, W. Wang, Y. Shangguan, Z. Cai, Z.-Y. Dong, Z. Huang, W. Si, Z. Ma, R. Kajimoto, K. Ikeuchi *et al.*, Neutron spectroscopy evidence on the dual nature of magnetic excitations in a van der waals metallic ferromagnet Fe$_{2.72}$GeTe$_2$, Phys. Rev. X **12**, 011022 (2022).

[12] J. Lee, S. Lee, J. H. Ryoo, S. Kang, T. Y. Kim, P. Kim, C. Park, J. Park, and H. Cheong, Ising-type magnetic ordering in atomically thin FePS$_3$, Nano Lett. **16**, 7433 (2016).

[13] Z. Ni, A. Haglund, H. Wang, B. Xu, C. Bernhard, D. Mandrus, X. Qian, E. Mele, C. Kane, and L. Wu, Imaging the Néel vector switching in the monolayer antiferromagnet MnPSe$_3$ with strain-controlled Ising order, Nat. Nanotechnol. **16**, 782 (2021).

[14] W. Klingen, G. Eulenberger, and H. Hahn, About hexathio- and hexaselenohypodiphosphate type M$_2^{II}$P$_2$X$_6$, Naturwissenschaften **55**, 229 (1968).

[15] B. Taylor, J. Steger, A. Wold, and E. Kostiner, Preparation and properties of iron phosphorus triselenide, FePSe$_3$, Inorg. Chem. **13**, 2719 (1974).

[16] A. Wiedenmann, J. Rossat-Mignod, A. Louisy, R. Brec, and J. Rouxel, Neutron diffraction study of the layered compounds MnPSe$_3$ and FePSe$_3$, Solid State Commun. **40**, 1067 (1981).

[17] K. Kurosawa, S. Saito, and Y. Yamaguchi, Neutron diffraction study on MnPS$_3$ and FePS$_3$, J. Phys. Soc. Jpn. **52**, 3919 (1983).

[18] K. Okuda, K. Kurosawa, S. Saito, M. Honda, Z. Yu, and M. Date, Magnetic properties of layered compound MnPS$_3$, J. Phys. Soc. Jpn. **55**, 4456 (1986).

[19] P. A. Joy and S. Vasudevan, Magnetism in the layered transition-metal thiophosphates MPS$_3$ (M=Mn, Fe, and Ni), Phys. Rev. B **46**, 5425 (1992).

[20] A. R. Wildes, S. J. Kennedy, and T. J. Hicks, True two-dimensional magnetic ordering in MnPS$_3$, J. Phys.: Condens. Matter **6**, L335 (1994).

[21] A. R. Wildes, B. Roessli, B. Lebech, and K. W. Godfrey, Spin waves and the critical behaviour of the magnetization in MnPS$_3$, J. Phys.: Condens. Matter **10**, 6417 (1998).

[22] A. R. Wildes, H. M. Rønnow, B. Roessli, M. J. Harris, and K. W. Godfrey, Static and dynamic critical properties of the quasi-two-dimensional antiferromagnet MnPS$_3$, Phys. Rev. B **74**, 094422 (2006).

[23] K. C. Rule, G. J. McIntyre, S. J. Kennedy, and T. J. Hicks, Single-crystal and powder neutron diffraction experiments on FePS$_3$: Search for the magnetic structure, Phys. Rev. B **76**, 134402 (2007).

[24] A. R. Wildes, K. C. Rule, R. I. Bewley, M. Enderle, and T. J. Hicks, The magnon dynamics and spin exchange parameters of FePS$_3$, J. Phys.: Condens. Matter **24**, 416004 (2012).

[25] D. Lançon, H. C. Walker, E. Ressouche, B. Ouladdiaf, K. C. Rule, G. J. McIntyre, T. J. Hicks, H. M. Rønnow, and A. R. Wildes, Magnetic structure and magnon dynamics of the quasi-two-dimensional antiferromagnet FePS$_3$, Phys. Rev. B **94**, 214407 (2016).

[26] L. Chen, X. Teng, D. Hu, F. Ye, G. E. Granroth, M. Yi, J.-H. Chung, R. J. Birgeneau, and P. Dai, Thermal evolution of spin excitations in honeycomb Ising antiferromagnetic FePSe$_3$, npj Quantum Mater. **9**, 40 (2024).

[27] A. R. Wildes, B. Fåk, U. B. Hansen, M. Enderle, J. R. Stewart, L. Testa, H. M. Rønnow, C. Kim, and J.-G. Park, Spin wave spectra of single crystal CoPS$_3$, Phys. Rev. B **107**, 054438 (2023).

[28] C. Kim, J. Jeong, P. Park, T. Masuda, S. Asai, S. Itoh, H.-S. Kim, A. Wildes, and J.-G. Park, Spin waves in the two-dimensional honeycomb lattice XXZ-type van der Waals antiferromagnet CoPS$_3$, Phys. Rev. B **102**, 184429 (2020).

[29] A. Scheie, P. Park, J. W. Villanova, G. E. Granroth, C. L. Sarkis, H. Zhang, M. B. Stone, J.-G. Park, S. Okamoto, T. Berlijn, and D. A. Tennant, Spin wave Hamiltonian and anomalous scattering in NiPS$_3$, Phys. Rev. B **108**, 104402 (2023).

[30] A. R. Wildes, V. Simonet, E. Ressouche, G. J. McIntyre, M. Avdeev, E. Suard, S. A. J. Kimber, D. Lançon, G. Pepe, B. Moubaraki, and T. J. Hicks, Magnetic structure of the quasi-two-dimensional antiferromagnet NiPS$_3$, Phys. Rev. B **92**, 224408 (2015).

[31] A. Bhutani, J. L. Zuo, R. D. McAuliffe, C. R. dela Cruz, and D. P. Shoemaker, Strong anisotropy in the mixed antiferromagnetic system Mn$_{1-x}$Fe$_x$PSe$_3$, Phys. Rev. Mater. **4**, 034411 (2020).

[32] S. Selter, Y. Shemerliuk, M.-I. Sturza, A. U. B. Wolter, B. Büchner, and S. Aswartham, Crystal growth and anisotropic magnetic properties of quasi-two-dimensional (Fe$_{1-x}$Ni$_x$)$_2$P$_2$S$_6$, Phys. Rev. Mater. **5**, 073401 (2021).

[33] M. J. Coak, D. M. Jarvis, H. Hamidov, A. R. Wildes, J. A. M. Paddison, C. Liu, C. R. S. Haines, N. T. Dang, S. E. Kichanov, B. N. Savenko et al., Emergent magnetic phases in pressure-tuned van der waals antiferromagnet FePS$_3$, Phys. Rev. X **11**, 011024 (2021).

[34] X. Ma, Y. Wang, Y. Yin, B. Yue, J. Dai, J. Cheng, J. Ji, F. Jin, F. Hong, J. Wang et al., Dimensional crossover tuned by pressure in layered magnetic NiPS$_3$, Sci. China Phys. Mech. Astron. **64**, 297011 (2021).

[35] S. Kang, K. Kim, B. H. Kim, J. Kim, K. I. Sim, J. Lee, S. Lee, K. Park, S. Yun, T. Kim et al., Coherent many-body exciton in van der Waals antiferromagnet NiPS$_3$, Nature (London) **583**, 785 (2020).

[36] K. Hwangbo, Q. Zhang, Q. Jiang, Y. Wang, J. Fonseca, C. Wang, G. M. Diederich, D. R. Gamelin, D. Xiao, J. Chu et al., Highly anisotropic excitons and multiple phonon bound states in a van der Waals antiferromagnetic insulator, Nat. Nanotechnol. **16**, 655 (2021).

[37] S. Liu, A. Granados del Águila, D. Bhowmick, C. K. Gan, T. Thu Ha Do, M. A. Prosnikov, D. Sedmidubský, Z. Sofer, P. C. M. Christianen, P. Sengupta, and Q. Xiong, Direct observation of magnon-phonon strong coupling in two-dimensional antiferromagnet at high magnetic fields, Phys. Rev. Lett. **127**, 097401 (2021).

[38] Y. Sun, J. Lai, S. Pang, X. Liu, P. Tan, and J. Zhang, Magneto-raman study of magnon-phonon coupling in two-dimensional ising antiferromagnetic FePS$_3$, J. Phys. Chem. Lett. **13**, 1533 (2022).

[39] J. Cui, E. V. Boström, M. Ozerov, F. Wu, Q. Jiang, J. Chu, C. Li, F. Liu, X. Xu, A. Rubio et al., Chirality selective magnon-phonon hybridization and magnon-induced chiral phonons in a layered zigzag antiferromagnet, Nat. Commun. **14**, 3396 (2023).

[40] G. Le Flem, R. Brec, G. Ouvard, A. Louisy, and P. Segransan, Magnetic interactions in the layer compounds MPX$_3$ (M = Mn, Fe, Ni; X = S, Se), J. Phys. Chem. Solids **43**, 455 (1982).

[41] P. Jeevanandam and S. Vasudevan, Magnetism in MnPSe$_3$: a layered 3d^5 antiferromagnet with unusually large XY anisotropy, J. Phys.: Condens. Matter **11**, 3563 (1999).

[42] S. Calder, A. V. Haglund, A. I. Kolesnikov, and D. Mandrus, Magnetic exchange interactions in the van der Waals layered antiferromagnet MnPSe$_3$, Phys. Rev. B **103**, 024414 (2021).

[43] T. T. Mai, K. F. Garrity, A. McCreary, J. Argo, J. R. Simpson, V. Doan-Nguyen, R. V. Aguilar, and A. R. H. Walker, Magnon-phonon hybridization in 2D antiferromagnet MnPSe$_3$, Sci. Adv. **7**, eabj3106 (2021).

[44] G. L. Squires, *Introduction to the Theory of Thermal Neutron Scattering* (Courier, New York, 1996).

[45] G. Shirane, S. M. Shapiro, and J. M. Tranquada, *Neutron Scattering with a Triple-axis Spectrometer: Basic Techniques* (Cambridge University Press, Cambridge, 2002).

[46] K.-Z. Du, X.-Z. Wang, Y. Liu, P. Hu, M. I. B. Utama, C. K. Gan, Q. Xiong, and C. Kloc, Weak van der waals stacking, wide-range band gap, and raman study on ultrathin layers of metal phosphorus trichalcogenides, ACS Nano **10**, 1738 (2016).

[47] R. Kajimoto, M. Nakamura, Y. Inamura, F. Mizuno, K. Nakajima, S. Ohira-Kawamura, T. Yokoo, T. Nakatani, R. Maruyama, K. Soyama et al., The Fermi chopper spectrometer 4SEASONS at J-PARC, J. Phys. Soc. Jpn. **80**, SB025 (2011).

[48] M. Nakamura, R. Kajimoto, Y. Inamura, F. Mizuno, M. Fujita, T. Yokoo, and M. Arai, First demonstration of novel method for inelastic neutron scattering measurement utilizing multiple incident energies, J. Phys. Soc. Jpn. **78**, 093002 (2009).

[49] Y. Inamura, T. Nakatani, J. Suzuki, and T. Otomo, Development status of software "Utsusemi" for chopper spectrometers at MLF, J-PARC, J. Phys. Soc. Jpn. **82**, SA031 (2013).

[50] R. A. Ewings, A. Buts, M. Le, J. van Duijn, I. Bustinduy, and T. Perring, Horace: Software for the analysis of data from single crystal spectroscopy experiments at time-of-flight neutron instruments, Nucl. Instrum. Methods Phys. Res., Sect. A **834**, 132 (2016).

[51] S. Toth and B. Lake, Linear spin wave theory for single-Q incommensurate magnetic structures, J. Phys.: Condens. Matter **27**, 166002 (2015).

[52] D. Jana, D. Vaclavkova, I. Mohelsky, P. Kapuscinski, C. W. Cho, I. Breslavetz, M. Białek, J. P. Ansermet, B. A. Piot, M. Orlita, C. Faugeras, and M. Potemski, Magnon gap excitations in van der Waals antiferromagnet $MnPSe_3$, arXiv:2309.06866.

[53] W. Nolting and A. Ramakanth, *Quantum Theory of Magnetism* (Springer Science & Business Media, Berlin, 2009).

[54] R. Takahashi and N. Nagaosa, Berry curvature in magnon-phonon hybrid systems, Phys. Rev. Lett. **117**, 217205 (2016).

[55] X. Zhang, Y. Zhang, S. Okamoto, and D. Xiao, Thermal hall effect induced by magnon-phonon interactions, Phys. Rev. Lett. **123**, 167202 (2019).

[56] T. Kikkawa, K. Shen, B. Flebus, R. A. Duine, K. I. Uchida, Z. Qiu, G. E. W. Bauer, and E. Saitoh, Magnon polarons in the spin seebeck effect, Phys. Rev. Lett. **117**, 207203 (2016).

[57] S. Bao, Z.-L. Gu, Y. Shangguan, Z. Huang, J. Liao, X. Zhao, B. Zhang, Z.-Y. Dong, W. Wang, R. Kajimoto *et al.*, Direct observation of topological magnon polarons in a multiferroic material, Nat. Commun. **14**, 6093 (2023).

[58] G. Go, S. K. Kim, and K.-J. Lee, Topological magnon-phonon hybrid excitations in two-dimensional ferromagnets with tunable Chern numbers, Phys. Rev. Lett. **123**, 237207 (2019).

[59] P. Shen and S. K. Kim, Magnetic field control of topological magnon-polaron bands in two-dimensional ferromagnets, Phys. Rev. B **101**, 125111 (2020).

[60] S. Zhang, G. Go, K.-J. Lee, and S. K. Kim, SU(3) topology of magnon-phonon hybridization in 2D antiferromagnets, Phys. Rev. Lett. **124**, 147204 (2020).

[61] C. Kittel, Physical theory of ferromagnetic domains, Rev. Mod. Phys. **21**, 541 (1949).

[62] C. Kittel, Interaction of spin waves and ultrasonic waves in ferromagnetic crystals, Phys. Rev. **110**, 836 (1958).

[63] B. Ma and G. A. Fiete, Antiferromagnetic insulators with tunable magnon-polaron Chern numbers induced by in-plane optical phonons, Phys. Rev. B **105**, L100402 (2022).

[64] S. Park, N. Nagaosa, and B. Yang, Thermal hall effect, spin nernst effect, and spin density induced by a thermal gradient in collinear ferrimagnets from magnon-phonon interaction, Nano Lett. **20**, 2741 (2020).

[65] D. C. Johnston, Magnetic dipole interactions in crystals, Phys. Rev. B **93**, 014421 (2016).

[66] W. Baltensperger and J. Helman, Influence of magnetic order in insulators on the optical phonon frequency, Helv. Phys. Acta **41**, 668 (1968).

[67] T. Huberman, R. Coldea, R. A. Cowley, D. A. Tennant, R. L. Leheny, R. J. Christianson, and C. D. Frost, Two-magnon excitations observed by neutron scattering in the two-dimensional spin-$\frac{5}{2}$ Heisenberg antiferromagnet Rb_2MnF_4, Phys. Rev. B **72**, 014413 (2005).

[68] R. A. Cowley, W. J. L. Buyers, P. Martel, and R. W. H. Stevenson, Two-magnon scattering of neutrons, Phys. Rev. Lett. **23**, 86 (1969).

[69] K. Park, J. Oh, J. C. Leiner, J. Jeong, K. C. Rule, M. D. Le, and J.-G. Park, Magnon-phonon coupling and two-magnon continuum in the two-dimensional triangular antiferromagnet $CuCrO_2$, Phys. Rev. B **94**, 104421 (2016).

[70] M. Songvilay, S. Petit, F. Damay, G. Roux, N. Qureshi, H. C. Walker, J. A. Rodriguez-Rivera, B. Gao, S.-W. Cheong, and C. Stock, From one- to two-magnon excitations in the $S = 3/2$ magnet $\beta-CaCr_2O_4$, Phys. Rev. Lett. **126**, 017201 (2021).